Addition of $Al(OH)_3$ vs. AlO(OH) nanoparticles on the optical, thermo-mechanical and heat/oxygen transmission properties of microfibrillated cellulose films

Tjaša Kolar
University of Maribor: Univerza v Mariboru
Branka Mušič
Nanotesla Institute Ljubljana
Romana Cerc Korošec
University of Ljubljana: Univerza v Ljubljani
Vanja Kokol (vanja.kokol@um.si)
Univerza v Mariboru https://orcid.org/0000-0002-8521-0941

Research Article

Keywords: Microfibrillated cellulose, Aluminum hydroxide nanoparticles, Transparent films, Mechanical properties, Thermal management, Oxygen and heat transmission.

Posted Date: April 2nd, 2021

DOI: https://doi.org/10.21203/rs.3.rs-340825/v1

Version of Record: A version of this preprint was published at Cellulose on August 12th, 2021. See the published version at https://doi.org/10.1007/s10570-021-04129-6.

Abstract

Differently structured aluminum (tri/mono) hydroxide ($Al(OH)_3$ / AlO(OH)) nanoparticles were prepared and used as thermal-management additives to microfibrillated cellulose (MFC), cast-dried in thin-layer films. Both particles increased the thermal stability of the MFC film, yielding 20–23% residue at 600 °C, and up to 57% lowered enthalpy (to 5.5–7.5 kJ/g) at 0.15 wt% of loading, while transforming to Al_2O_3. However, the film containing 40 nm large $Al(OH)_3$ particles decomposed in a one-step process, and released up to 20 % more energy between 300–400°C as compared to the films prepared from smaller (21 nm) and meta-stable AlO(OH), which decomposed gradually with an exothermic peak shifted to 480 °C. The latter resulted in a highly flexible, optically transparent (95%), and mechanically stronger (5.7 GPa) film with a much lower specific heat capacity (0.31 – 0.28 J/gK compared to 0.68–0.89 J/gK for MFC-$Al(OH)_3$ and 0.87–1.26 for MFC films), which render it as an effective heat-dissipating material to be used in flexible opto-electronics. Low oxygen permeability (2192.8 cm^3/m^2day) and a hydrophobic surface (>60°) rendered such a film also useful in ecologically-benign and thermosensitive packaging.

1. Introduction

Nano and micro-fibrillated cellulose produced from renewable resources is becoming an important biodegradable, low cost and lightweight material (Klemm et al. 2018). This is also related to its significant physical and chemical properties, above all, high crystallinity, low density, extraordinary mechanical properties and nanoscale dimension, that gives high surface area and huge amounts of hydroxyl groups available for hydrogen bonding or specific chemical modification (Dufresne 2013; Klemm et al. 2018). Its application expands from the production of packaging, paper and board, to flexible films, acting as thermal insulators, as well as a functional material for forthcoming cutting-edge applications in electronics (Abitbol et al. 2016), energy storage (Kim et al. 2019; Beeran et al. 2016), electromagnetic interference shielding (Gopakumar et al. 2018; Zeng et al. 2020), solar cells (Du et al. 2017), photo/catalysis (Kaushik and Moores 2016) etc. where it acts mainly as a template or carrier for functional in/organic nanoparticles like carbon nanotubes (Miyashiro et al. 2020), graphene oxide (Beeran et al. 2016; Wicklein et al. 2014), metal nanoparticles (Oun et al. 2020; Kaushik and Moores 2016), thus giving the products high added-value properties by acting synergistically.

High optical transparency with good thermal stability and low heat transmission properties are important features of such functional cellulose based materials, rendering their final applications. On the other hand, toxicological concerns and ecological acceptability and handling of such materials after use are becoming an increasingly important factor. Many recent studies have, thus, focused on the application of nanoparticles based on silicon (Mastalska-Popławska et al. 2017; Li et al. 2017; Lin et al. 2018), minerals (montmorillonite (Köklükaya et al. 2017), carbonate (Farooq et al. 2018), kaolinite (Castro et al. 2018), hydroxyapatite (Guo et al. 2018), sepiolite (Ghanadpour et al. 2018)), magnesium derivatives (Jiang et al. 2019), or their combinations (Köklükaya et al. 2017; Wang et al. 2018; Li et al. 2017).

Among the inorganic and environmentally benign nanoparticles, **aluminum (tri) hydroxide ($Al(OH)_3$)** (He et al. 2018) is becoming one of the most significant and inexpensive alternatives. ATH is an amphoteric mineral, the morphological crystalline structure of which depends on the synthesis route, and can, thus, exist in four polymorphs, among which the gibbsite is the most relevant, followed by three much rarer forms of bayerite, doyleite and nordstrandite (Karger-Kocsis and Lendvai 2018). ATH acts in the condensed phase, where it decomposes endothermically (at about 180–200°C) (Laoutid et al. 2009), whereby it absorbs 594 kJ/mol of energy/heat, and forms aluminum oxide, together with the release of water molecules, according to Eq. 1:

$2Al(OH)_3 \rightarrow Al_2O_3 + 3H_2O$ Eq. 1

These dilute combustible gases reduce the burning temperature, and prevent the access of oxygen by formation of a protective ceramic or vitreous layer on the surface from the residual crystalline polymorphic phase of aluminum oxide (Al_2O_3), thus improving its thermal stability (Hull et al. 2011; Laoutid et al. 2009). The effect of ATH thermal stability is increased by decreasing the particle size (He et al. 2018) and increasing its concentration (Hull et al. 2011) and dispersibility (Norouzi et al. 2015), which, however, influence the product`s mechanical properties and transparency (Beyer 2001).

Aluminum (mono) hydroxide (AlO(OH)), known as boehmite, is another closely related ATH nanoparticle structure with well crystallized orthorhombic unit cells, which is turned into nanocrystalline γ-Al_2O_3 forms by a topotactic transformation throughout the heating. The endothermic reaction starts between 400–700°C, during which 257 kJ/mol of energy/heat is absorbed (Karger-Kocsis and Lendvai 2018), according to Eq. 2:

$$2AlO(OH) \rightarrow Al_2O_3 + 2H_2O \qquad \text{Eq.2}$$

The abundant surface decorated peripheral OH functional groups of both ATH particles offer, in addition, good dispersion and filler/matrix adhesion properties (De Salvi et al. 2012).

The aim of the presented work was, thus, to examine the effect of structurally and morphologically different ATH nanoparticles (**$Al(OH)_3$ vs. AlO(OH)**), their dispersibility and loading quantity on the thermal stability and heat transmission properties of the films prepared from microfibrillated cellulose (MFC), thus to define their limitation in higher temperature and heat resistant applications. The films' structural, optical, mechanical, wetting, and oxygen permeability were also examined.

2. Experimental

2.1. Materials used

1.9 wt% water suspended wood-based microfibrillated cellulose (MFC, Exilva F-01-L, Borregaard AS, Norway), consisting of 22–50 µm long and up to 100 nm tight fibrils with negative surface charge of − 28 ± 2.2 mV and 18.5 ± 4.0 mmol/kg, as determined by using conductometric titration, were used through the study. The 16–21 µm sized $Al(OH)_3$ particles were purchased from Kemipal-W 900, Kemira KTM, Slovenia. Aluminum isopropoxide (Al(O-i-Pr)3), 2-propanol, acetic acid, 2-octanol, and polyethylene glycol 400 were purchased form Sigma-Aldrich, USA. Dolapix ET 85 (the dispersing agent) was obtained from Zschimmer and Schwarz Inc, Germany).

2.2. Preparation of ATH nanoparticles

Water based ATH nanoparticles (**$Al(OH)_3$ - ATHw**) were prepared from commercially available micro-sized $Al(OH)_3$ particles by the two-stage grinding process. For ATH40w particles` preparation, the grinding balls (Yttria-stabilized zirconia, Yotai Refractories Co. Ltd, Japan) with a diameter of 2 mm, distilled water, commercially bought $Al(OH)_3$ and polyethylene glycol as a dispersant were weighed into an agate grinding bowl of the Planetary Mill (Pulverisette 5 classic line, FRITSCH GmbH, Germany) in the mass ratio of 1 : 1 : 0.35, and grinded for 60 minutes at 280 rpm. The grinding balls were then replaced with ones having a diameter of 0.5 mm, and 2-octanol (antifoaming agent) was added to grind the particles for another 60 minutes at 320 rpm. For the ATH50w nanoparticle preparation, the antifoaming agent (2-octanol) and deflocculant (Dolapix ET 85) were added at the first stage of grinding, followed by the second stage as described above for the preparation of ATH40w nanoparticles.

Propanol based ATH nanoparticles (**AlO(OH)** - **ATHp**) were prepared by the sol-gel procedure according to our previous study (Bunderšek et al. 2016). Briefly, aluminum isopropoxide ($Al(O\text{-}i\text{-}Pr)_3$) was added to 2-propanol as a carrier media and stirred. The mixture was then heated to 82°C, to the boiling point of 2-propanol, and then refluxed to become a clear slurry. Acetic acid as a catalyst and distilled water were added to the slurry to perform hydrolysis. The reaction was kept at temperature for 60 minutes, and amorphous ATH was produced as a result. Then the ATH was peptized and crystallized by refluxing for 20 hours. The mol ratio of reactants of Al(O-i-Pr)□: 2-propanol : acetic acid : water was 1 : 25 : 0.1 : 6. Distilled water was added at room temperature (20°C) to obtain 20 nm sized particles (ATH20p), where, for the 30 nm sized ones, the distilled water was heated to 40°C (ATH30p).

The prepared nanoparticles were designated as ATH40w, ATH50w, ATH20p, and ATH30p, where the number denotes its average size (40 nm, 50nm, 20 nm, 30 nm), while “w” or “p” means water or propanol used as the medium for synthesis, respectively.

2.3. Preparation of the films

The 1.9 wt% water suspended MFC was first diluted by distilled water to 0.3 wt% suspension and homogenized for 4 min with an Ultra Turax at 10000 rpm. To such prepared MFC dispersion, different weights of ATH nanoparticles (10 w/w%, 30 w/w% and 50 w/w%) according to the dry weight of MFC were added, by mixing it for 15 min with a magnetic stirrer at 1200 rpm, thus yielding final ATH mixture contents of 0.03 wt%, 0.09 wt% and 0.15 wt%, respectively. 50 ml of each dispersion was poured onto the Petri dish and air-dried at room temperature until the film was formed. The maximum amount of ATH nanoparticles` addition to MFC was chosen according to the film-forming ability. A sample prepared from MFC without nanoparticles was used as a reference. The composite films were designated according to the amount and type of ATH nanoparticles added and their dispersing medium, where the first number (1, 2 or 3) denotes the addition of ATH particles (1–10 w/w%, 2–30 w/w% and 3–50 w/w%), and the second their average size (20 nm, 30 nm, 40 nm or 50nm), while “w” or “p” means water or propanol used as a medium, respectively. For example, MFC-3-ATH20p means 0.3% MFC with 50w/w% added ATH nanoparticles synthesized in propanol with average size of 20 nm.

2.4. Characterization of ATH nanoparticles

X-Ray Diffraction (XRD; Miniflex II, Rigaku Corporation, Tokyo, Japan) was used to examine the crystallographic structures of the ATH particles.

The Dynamic Light Scattering (DLS) technique (Horiba LB 550, Japan) was used to determine the average size of the ATH nanoparticles.

Specific Surface Area (SSA) was measured with a Surface Area and Porosity Analyzer (Micrometrics Tristar 3000, Micromeritics, Norcross, GA, USA) by using nitrogen adsorption-desorption and a Brunauer–Emmett–Telle model, where SSA was determined by calculating the amount of absorbed nitrogen gas, corresponding to a monomolecular layer of nitrogen on the surface of the sample, and consideration of the nitrogen SSA (0.162 nm^2), as a function of relative pressure. The samples were dried before analyses (HG63, Mettler Toledo) at 105°C for 60 minutes.

The morphology and elementary structure of the ATH nanoparticles was characterized by using a Scanning Electron Microscope, Sirion 400NC (FEI, USA), equipped with an Energy-Dispersive X-ray spectroscope, INCA 350 (Oxford Instruments, UK).

The Thermo-Gravimetric Analysis (TGA) was conducted using a DSC1 analyzer, (Mettler Toledo, Switzerland), and Differential Scanning Calorimetry (DSC) was performed using a DSC823e Module STARe System (Mettler Toledo, Switzerland). Aluminum pans with pierced lids, containing ~40 mg of ATH samples for TGA analysis and ~22 mg of ATH samples for DSC analysis, were analyzed in an air atmosphere with a temperature rate of 10°C/min from 25°C to 600°C.

2.5. Characterization of the films

SEM imaging of the films was performed using a Sirion 400NC (FEI, USA) microscope to study the morphology and nanoparticle distribution.

Fourier Transform Infrared (FTIR) spectra of the films were recorded by using a Perkin-Elmer Spectrum One spectrometer (US). The transmission measurements were carried out in the range of 400–4000 cm^{-1} with 16 scans and a resolution of 4.0 with interval 1 cm^{-1}. The Spectrum 5.0.2 software program (version 10.6.1.) was applied for the data analysis.

The transmission vs. reflection of the films was recorded within the 250–750 nm wavebands by using a Lambda 900 UV-Vis spectrophotometer (Perkin Elmer, USA) with an integrating sphere and scanning speed of 450 nm min^{-1}.

Contact Angle (CA) measurements of the films were performed using an SCA20 Contact Angle measurement system (Goniometer OCA 35, Dataphysics, Germany). All measurements were conducted at room temperature on both sides of the films, with milliQ water used as the test liquid, volume of 3 mL. Each CA value was the average of at least six drops of liquid per surface, where at least three measures were made for each side of the film.

The oxygen permeability of the films was measured using a Perme OX2/230 Oxygen Transmission Rate Test System (Germany), and the results evaluated by the software program WinPerme OX2-230 W3-330. All measurements were conducted at a temperature of 23 ± 0.1°C and 50 ± 1% humidity. Four measurements were performed for each tested sample.

The tensile strength properties of the films were performed using a Shimadzu AGS-X electromechanical universal testing machine (Japan) according to the Standard ISO 6892-1:2009(E). The (55 mm long) samples were cut into a paddle shape (10 mm width of the wide part and 15 mm length of the wide part – on each side, with 3 mm width of the narrow part in the middle and 19 mm length of the narrow part), attached to clamps at a distance of 30.8 mm and tested at a speed of 0.05 mm/s. Three measurements were performed for each tested sample.

Thermo-Gravimetric Analysis (TGA) and Dynamic Scanning Calorimetry (DSC) measurements of the films were performed using a Mettler-Toledo DSC1 instrument (Switzerland) under air atmosphere in a temperature range from 25 to 600°C and the heating rate of 10°C/min, using a 50 mL/min of flow rate. For TGA analysis a 150 µL platinum crucible was used, and the initial mass of samples (4–5 mg) being cut with scissors to suitable dimensions. The blank curve was subtracted in all measurements. For DSC measurements, the samples (0.5–1.0 mg), weighed carefully in a 20 µL light aluminum pan on an external Mettler Toledo MX5 balance, were pressed to the bottom of the crucible with a Teflon rod with a pierced lid, to provide contact during all the measurement and, thus, prevent the undesirable loss of the DSC signal. An empty aluminum pan served as a reference.

Quasi-static specific Heat Capacity was studied by a new temperature modulated DSC technique - TOPEM, introduced by Mettler-Toledo, using a Mettler Toledo DSC1 instrument (Switzerland) (Schawe et al. 2006). The measurements were performed under multi-frequency temperature-modulated conditions in a temperature range from 20°C to 240°C, and heating rate of 1°C/min and a modulation amplitude of ± 0.5°C. Samples with initial masses from 2 to 3 mg (approx. 5 stacks of a round-cut film) were placed into a 20 µL aluminum crucible and covered with a lid, which was pressed down firmly with a Teflon rod. An empty crucible served as a reference.

3. Results And Discussion

3.1. Structural, morphological and thermal properties of synthesized ATH nanoparticles

The structure and thermal properties of the prepared ATH nanoparticles were evaluated using different analytical techniques.

SEM images (Fig. 1a) showing the different morphological features of the synthesized ATH nanoparticles: Uniformly distributed and mostly plate/flat structured ATHw, and smaller spherical shaped ATHp particles. XRD diffractograms (Fig. 1b) of ATH nanoparticles, indicated that the ATHw particles had a mixed crystal phase of predominantly monocline gibbsite ($Al(OH)_3$) and meta-stable orthorhombic boehmite (aluminum oxide hydroxide, AlO(OH)) (Reddy et al. 2014), being reflected in well-defined narrow sharp peaks between 18° and 22° and some broader peaks at higher 2-theta (JCPDS No. 33 – 0018), respectively. On the other hand, weak broad peaks between 10° and 30°, characteristic of the boehmite (AlO(OH), and the two sharp reflections at around 37° and 44° with small shoulder at around 66° characteristic for bayerite (Al_2O_3), were indicated for ATHp particles, as already confirmed by our previous study (Bunderšek 2015; Bunderšek et al. 2016). The difference in the crystalline structure is supported by the elemental compositions (Table 1), that confirmed the presence of different weight mass of oxygen and aluminum, as well as the formation of hybrid structures with different O/Al ratios (1.27 for ATH20p and 1.90 for ATH40w). DLS (Fig. 1c) and BET (Fig. 1d, Table 1) analysis indicated that the ATHw particles were much larger (~39.6 nm / ATH40w and ~49.7 nm / ATH50w) with an SSA of 18.9 m^2/g and 59.5 m^2/g, respectively, compared to ATHp particles (ATH20p and ATH30p), being in the range of 21.7–31.9 nm, and possessing much higher, but comparatively similar SSA (385.4 m^2/g and 377.7 m^2/g). According to the nitrogen adsorption-desorption isotherms (Fig. 1d), the pore diameter of the ATHw samples is in the range of 14.9–15.9 nm and ATHp based around 6.7 nm, which means that the pores of both types of particles are classified as mesopores (range 2–50 nm) (Sing 1985). The nitrogen adsorption-desorption hysteresis loop performed on the samples showed a type IV isotherm, which is associated with capillary condensation taking place in the mesopores. However, there was a big difference between the steepness and width of the isotherms for ATHw *vs.* ATHp particles. The hysteresis loop of ATHw based samples was very steep, almost vertical, which points to agglomerates or spherical particles arranged in a uniform way, and facile pore connectivity. On the other hand, ATHp samples had a wider and more gradual slope, indicating aggregates and slit shaped pores with good connectivity.

Table 1
Structural and thermal properties of different ATH nanoparticles

Particle designation	ATH40w	ATH50w	ATH20p	ATH30p
Average size [nm]	39.6	49.7	21.7	31.9
Specific surface area [m^2/g]	18.9	59.5	385.4	377.7
Pore diameter [nm]	14.9	15.9	6.7	6.7
Pore volume [cm^3/g]	0.07	0.28	0.91	0.89
Weight loss 25–100°C [%]	0.6	0	14.1	18.2
Additional weight loss 200–400°C [%]	29.9	29.5	7.3	7.6
TGA residue at 600°C [%]	67	67.5	69.5	65.4
Enthalpy [J/g]	-876.4	-752.9	-245.3	-235.2
Al [wt%]	34.39	n.d.	43.94	n.d.
O [wt%]	65.61		56.06	
O/Al	1.908		1.276	
O/Al at 600°C	1.142		1.261	

The thermal properties of the synthesized ATH nanoparticles, evaluated by thermal decomposition in an air atmosphere between 25°C and 600°C (Fig. 2c), indicated that the amount of residue at 600°C for both types of nanoparticles (ATHw and ATHp) were almost the same (from 65.4–69.5%). However, thermal degradation of ATHp nanoparticles occurs in two steps, while ATHw ones in one step, where most of the weight loss (29%) occurs in the range of 250–320°C, attributed to the transformation from $Al(OH)_3$ to Al_2O_3 according to Eq. 1, or via AlO-OH (Favaro et al. 2010; Lamouri et al. 2017), and, up to 600°C, an additional 5% of weight is lost. On the other hand, the ATHp particles start to degrade soon after the temperature is increased, resulting in a weight loss of 14.1% (ATH20p) – 18.2% (ATH30p) in the range of 25–200°C, due to topotactic transformation of the meta-stable boehmite phase (release of one mole of water; Karger-Kocsis and Lendvai 2018), while only 7% of additional weight is lost in the range of 200–400°C, and an additional 9% up to 600°C, indicating its gradual change into nanocrystalline Al_2O_3 forms with smoother crystalline structure (Fig. 2a). When exposed to elevated temperatures, all types of tri/mono-hydrated alumina nanoparticles thus transform to γ-Al_2O_3, which is shown with almost equal XRD diffractograms (the main characteristic peaks at around 38°, 45° and 67°; Sifontes et al. 2014; Rahmanpour et al. 2012; Fig. 2b), as well as similar elemental compositions (Table 1), but slightly different O/Al ratio (1.14 vs. 1.26), which might be due to the different kinetic of transformation and formation of structurally different polymorphs of alumina. The slower degradation rate of ATHp particles at higher temperatures, meaning better thermal stability, which can also be reflected from the DSC analysis (Fig. 2d) and calculated relevant enthalpy values, are collected in Table 1. According to the different path and mode of thermal transformation (Eqs. 1 and 2), much more energy is, thus, released during the decomposition of ATHw nanoparticles (876.4 J/g for ATH40w and 752 J/g for ATH50w) as compared to the ATHp ones (245.3 J/g for ATH20p and 232.2 J/g for ATH30p). The smaller and nanocrystalline-structured ATHp particles with numerous H-bonding and internally adsorbed water molecules, thus release less energy to transform in minority present boehmite (AlO(OH)) structures and further into fully dehydrated Al_2O_3 forms, where, on the contrary, ATHw particles need much more energy to be transformed from predominant gibbsite ($Al(OH)_3$).

3.2. Surface morphological and physico-chemical properties of the films

The surface morphology and physico-chemical properties of the nanocomposite films were studied by SEM imaging, Contact Angle measurements, FTIR and UV-Vis spectroscopy.

A fibrillated and ribbon shaped structure is seen from the **SEM imaging** (Fig. 3a) for the pure MFC film, which is preserved even with the addition of the highest percentage (50 w/w%) of ATH nanoparticles but, however, gives differently distributed and dense films. Slightly aggregated, but uniformly and individually distributed ~40 nm large ATHw nanoparticles can be observed through the entire film (Fig. 3b), interacting well with the rare negative surface charge and huge -OH groups of cellulose backbone, and, thus, covering the surface of the cellulose fibrils fully. On the other hand, the areas of denser cellulose fibrillar net structures containing well dispersed ~20 nm large ATHp particles with intermediate free spaces were observed (Fig. 3c). Such an effect might be due to the use of faster volatile 2-propanol as a dispersing media for ATH particles, which induced attractive interactions between the fibril's -OH groups, acting as a glue, and thus inducing phase separations between the water-rich (98.3%) and alcohol-rich (17.9%) gelation regions of the cellulose microfibrils (da Silva et al. 2018), yielding nanostructured and inhomogeneous clustering of microdomains of the MFC containing ATHp particles. Optionally, ATHp particles consisting of two double layers of aluminum centered distorted octahedra $AlO_4(OH)_2$ forms, may also get separated by the hydrogen bond interaction between the AlO(OH) inter-layer OH and cellulose -OH groups after mixing (De Salvi et al. 2012), and exfoliate on the fibrils` surface during drying.

FTIR spectra of MFC-based films containing 50 w/w% of ATH particles (ATH40w, ATH20p) are presented in Fig. 4, and compared with those of pure MFC film to confirm the interactions between the components. The FTIR spectra of ATH40w particles show typical four mode peaks over the range of 3620 – 3380 cm^{-1}, being related to the stretching of OH groups that are interacting with the Al atoms (He et al. 2018), and being supported by Al-O stretching at ~1020 cm^{-1} (Gorgieva et al. 2020), corresponding to the predominant $Al(OH)_3$ structure. On the other hand, ATH20p has a much larger and broader peak for asymmetric and symmetric OH stretching vibrations centered at ~3300, with a small shoulder at ~2900 cm^{-1}. Absorption bands appeared at ~1637 cm^{-1} (assigned to the stretching and bending modes of the adsorbed water molecules), as well as a string band at ~1065 cm^{-1} with a small shoulder at ~1160 cm^{-1} (assigned to

the bending and wagging of the H bonds in the octahedral structure of OH-Al = O), at ~746 cm^{-1} (attributed to the stretching vibrations of Al-O-Al in the distorted AlO_6), at ~664 cm^{-1} and ~559 cm^{-1}, which are consistent with the reported values for a boehmite AlO(OH) structure (Abdollahifar et al. 2018) and the crystalline structures of Al_2O_3 defined by the XRD analysis (Fig. 1a).

The FTIR spectrum of pure MFC film shows typical cellulose bands: A broad band at ~3323 cm^{-1} for hydrogen bonded OH stretching, at ~2892 cm^{-1} for CH stretching, at ~1640 cm^{-1} for OH bending of absorbed water, at ~1420 cm^{-1} for CH_2 bending, at ~1026 cm^{-1} for C-O bending, and at ~897 cm^{-1} for CH or CH_2 stretching (Lu et al. 2008; Gorgieva et al. 2020). The presence of ATH40w in the MFC intensified its peak related to the OH groups over the range of 3616 – 3349 cm^{-1}, also showing three shoulders typical for Al-OH interactions on its backbone, as well as a characteristic peak for Al-O stretching of ATH40w at ~1018 cm^{-1} (Gorgieva et al. 2020). This may indicate the hydrogen bonding between the –OH groups of ATH particles and the cellulose backbone of MFC, covering the fibrils` surfaces. All the mentioned OH related peaks (in the range of 3600 – 3300 cm^{-1}) are not present on a broader and much smaller band, shifted to ~3314 cm^{-1}, in the case of MFC-ATH20p based film, on which bands characteristic for ATH20p are overlapping with those typical for cellulose structures, so they cannot be distinguished in the spectra. However, the hydrogen bond interactions between the –OH groups of MFC and–OH groups of AlO(OH) nanoparticles or oxygen of Al_2O_3, as well as between the ATH particles themselves, resulting in the presence of Al-O, according to the separation mechanism of octahedra $AlO_4(OH)_2$ forms as described above.

To support the finding of the chemical composition and topology of the films` surfaces, the **wetting properties** of the films were evaluated by measuring the Contact Angles (CA) using milliQ water. A larger CA indicates low surface energy and higher hydrophobicity (Wu et al. 2014). As seen from the results presented in Fig. 5, the addition of ATH nanoparticles to MFC changed its original CA value significantly (~43°), which is in the range for the other cellulose based films (from 28° (Andresen et al. 2006) to 60° (Belbekhouche et al. 2011)), confirming its high hydrophilicity due to the presence of many OH groups on its surface. The addition of ATH40w and ATH50w to MFC additionally lowered the CA of such a film to around 32°-33° at the highest (50 w/w%) concentrations, which might be due to the presence of additional highly hydrophilic -OH groups arising from the presence of ATHw particles fully covering the cellulose fibrils, as confirmed with the FTIR spectra and SEM analysis. On the other hand, the CA was increased up to ~68° for films prepared with 50 w/w% of ATH20p and ATH30p particles, also being in an agreement with their SEM and FTIR analyses (i.e. reduced -OH groups on MFC-ATHp microdomains). In addition, the volatile 2-propanol present in ATHp during film preparation, preferentially goes to the surface and, consequently, lowers the surface energy, making it more hydrophobic (Ballal and Chapman 2013). It is also worth mentioning that when water droplets were dripped onto the surface of such films, the droplets spread around the surface, but did not soak into the surface totally, as well as did not induce the films` dissolution due to the presence of water. A small difference in the mean CA values between both surfaces can be observed in the case of MFC-ATH-30p film, given ~72° on the upper-side and ~66° on the lower-side. This might be due to a difference in the film surface roughness and smoothness of the formed MFC-ATHp microdomains, as be seen from the SEM images, where a rougher surface gives higher CA than smoother ones due to the heterogeneous wetting being related to the formation of air compartments between the droplets and the surface (Beeran et al. 2016).

To get a better insight into the bulk nanostructure of such films, optical properties and Oxygen Transmission Rate (OTR) were evaluated of the MFC films containing different contents of ATH nanoparticles. The **transmittance values** (Fig. 6) of pure and thinner (19.2 µm) MFC films were the highest, and almost constant within all the wavelength ranges (from 98.9% at 400 nm to 93.4% at 700 nm), indicating that the films were fully transparent. The addition of ATH nanoparticles reduced the transmittance and increased the thickness, which is, however, highly dependent on the dispersibility, the crystalline structure and the size of the ATH nanoparticles (Acharya et al. 2018). With the formation of aggregates, particles get larger and, consequently, scatter the light more than the original small particles. The transmittance reduction is, thus, significant for 21–28 µm thin MFC-ATHw films (from about 86% to about 25–48% at 30 and 50 w/w% of ATH addition, respectively), while its changing in the case of MFC-ATHp films is much smaller (between 96.8–89.4%) compared to the pure MFC film, although they are thicker (23–32 µm) and more dependent on the particle size than on their content. The reason for such a difference could be in the different crystalline structure, morphologically larger (40–48 nm), lower SSA (18.9–59.5 m^2/g), aggregated and less uniform ATHw nanoparticles than ATHp ones (21–31 nm), with much higher SSA (385.4-377.7 m^2/g), which, consequently, blocks the light transmission (Sathish et al. 2015). This can also be supported by increasing the transmittance values by increasing the wavelength for both MFC-ATHw films (from 47% and 35% at 400 nm to 59% and 49% at 700 nm for MFC films containing ATH40w and ATH50w, respectively). As such, films are also more hydrophilic, adsorbing more moisture, and with the presence of $Al(OH)_3$ form-based particles, in addition increases the volume of voids between the fibrils.

OTR values of films thus also decreased from ~6622 cm^3/m^2day for pure MFC film to ~3600 cm^3/m^2day and ~2190 cm^3/m^2day for MFC-3-ATH30p and MFC-3-ATH20p, respectively, which is related primarily to the nanoparticles$structures\ \text{and}\ ,\text{sec}ondly,\ \rightarrow thefilms$ thicknesses; the films made of ATHw nanoparticles are approximately 10 µm thicker than pure MFC film, for which the OTR value exceeds the measuring range.

3.3. Mechanical properties of the films

Tensile testing of the films was performed to identify the effect of type and content of nanoparticles` addition to MFC film by measuring **tensile strength and Young's modulus** (Fig. 7). An increase of tensile strength up to 7.7–18.9% for the films containing up to 30 w/w% addition of ATHw nanoparticles, and its decrease by ~3.7% by further increase of its content to 50 w/w%, as compared to the pure MFC film (~59.2 MPa), can be observed, with the elastic modulus following the same trend. On the other hand, a slightly different behavior was noticed for the films containing ATHp particles. While a small reduction of both tensile strength (to ~44–47 MPa, 20–25%) and Young's modulus (from 3.6 GPa to ~2.8–3.3 GPa, 9–21%) were measured for the films containing the lowest (10 w/w%) ATHp content, as compared to the reference (pure MFC film), its increase to ~69 MPa (17%) and ~5.7 GPa (55%), respectively, by further addition of ATH20p (up to 50 w/w%), but slight decrease (4.7 MPa / 19%) was obtained in the case of using ATH30p. The results support the previous findings, indicating the effect of ATH morphology, size and crystalline structure, which, altogether, attribute to (part or full), coverage of cellulose fibrils` surfaces, and result in differently nanostructured films. Smaller (~21 nm) and well dispersed ATH20p particles with large surface area (385.4 m^2/g) thus result in more hydrogen bindings and dense connections inside the films.

3.4. Thermal stability of the films

Different techniques of TGA/DSC were used to evaluate the films' **thermal properties** in an air atmosphere and temperature range from 25°C to 600°C, including degradation temperature, residue amount after degradation, enthalpy, and specific heat capacity.

As presented in Fig. 8a, thermal degradation of pure MFC occurs in three successive steps: From room temperature to approximately 230°C, evaporation of physically adsorbed water takes place. In a temperature range from 230°C to 350°C weight loss is related to the collapse of the glucosidic structure and the formation of carbonyl compounds, which decompose completely at around 600°C (Lichtenstein and Lavoine 2017). The addition of ATH nanoparticles changed the course of thermal decomposition of pure MFC, depending on the type of ATH used. About a ≈3.5% larger weight loss in the case of MFC-ATH20p films (≈6.6%) compared to the MFC-ATH40w ones, (≈2.9%) up to 200°C was related to the different phase transformations of the used particles, as explained previously under the first Section. However, comparing the onset decomposition temperatures of the second step shows that MFC-ATH20p film (305°C) was the most thermally stable, followed by pure MFC (281°C) and MFC-ATH-40w as the less stable (260°C). The inflection point of both nanocomposite films occurred at around 330°C, given a weight loss of around 60% in the case of MFC-ATH40w, and around 40% for MFC-ATH20p films, while, for the pure MFC sample, this temperature was at around 350°C with ≈59% of weight loss. The addition of ATH nanoparticles also had a noticeable effect on the amount of residue after thermal decomposition, which increased from ~1.8% for pure MFC film to around 10% already with 30 w/w% addition of ATH40w and ATH20p, and further, to even ~20–23% for films containing the highest (50 w/w%) ATH concentrations, which is comparable with the other cellulose based materials containing different ATH nanoparticles (Gorgieva et al. 2020; Zhang et al. 2017; Yang et al. 2017). The higher residue amount means that the ATH nanoparticles had suppressed the film' degradation successfully with the dilution of radicals in flame, while the residue of alumina formed the protective layer (Hull et al. 2011). Some additional differences during the films` thermal decomposition can be seen from the comparison of their **derivative weight (DTG) curves** (Fig. 8b). Decomposition of the films with incorporated ATH40w particles occurs via three steps; the first one from 230°C to 280°C, which occurs only in these samples. The DSC curves of these samples (Fig. 8c) show that this process is endothermic, being assigned to the dehydration of $Al(OH)_3$ and AlO(OH) structures. In case of MFC films prepared with ATH20p, the dehydration and thermal decomposition of the organic MFC matrix takes place simultaneously. It is also obvious from the DTG curves that the maximal rate of glucosidic degradation was faster when nanoparticles were added to the MFC, while the second step was much slower. Some relevant data about the thermal decomposition process of the studied samples are collected in Table 2. Shifted onset decomposition to higher temperature, weight loss at the inflection point and lower rate of decomposition in the second step, show that ATH-20p films possess better thermal stability regarding the other MFC-ATHw or pure MFC films.

Table 2
Relevant data about the thermal decomposition process of different MFC-based films and Specific heat capacity (Cp) values at certain temperatures.

		MFC	ATH40w			ATH20p		
			3	2	1	3	2	1
Weight loss 25–200°C [%]		4.94	2.96	3.58	3.71	6.57	6.36	4.21
Onset decomp. temp. (2nd step) [°C]		281	260	262	279	305	305	307
Residual weight at 600°C [%]		1.8	23.3	17.1	10.1	20.1	12.6	9.9
Enthalpy [J/g]		13100	5576	5918	10700	7598	8385	9588
Enthalpy change (in regard to MFC) [%]		/	-57	-55	-18	-42	-36	-26
Position of main exothermic peak [°C]		479	338	336	419	466	479	481
Cp values at certain temp. [J/gK]	20°C	0.87	0.68	1.37	1.37	0.31	0.81	1.02
	100°C	0.97	0.68	1.65	1.48	0.26	0.93	1.41
	150°C	1.14	0.81	1.87	1.69	0.29	1.06	1.70
	200°C	1.26	0.89	1.93	1.90	0.28	1.09	1.93

In addition, the integrated values of the heat flow (Fig. 8c) show that **the enthalpy** of pure MFC film was reduced by about 57% (MFC-ATH40w) and 42% (MFC-ATH20p) (from ~13100 J/g to ~5576 J/g and ~7598 J/g, respectively), for the samples containing the highest (50 w/w%) amount of ATH nanoparticles. Decreased enthalpy values are related to less released energy in the process of burning, and, thus, its contribution to heating the film in the process of degradation was smaller. It is even more obvious from the comparison of DSC curves that the decomposition process differed as to whether ATHp or ATHw particles were added to the MFC. In the case of ATHp particles, the shape of the DSC curves was similar to MFC, and the process was the most exothermic in the second step of decomposition. Besides the initial endothermic reaction at the beginning of thermal decomposition at 230°C, already mentioned before, films with the addition of ATHw released much more heat in the temperature region from 300°C to 380°C (the exception was the film prepared with lowest ATH

content, where it followed the MFC curve, meaning that 10 w/w% ATH content was too low for making an observable difference). In the second step, much less heat was released compared to pure MFC and films prepared with the addition of ATHp nanoparticles, where most of the released heat was present in the temperature range 400–500°C. Such an effect might be due to the one step transformation from AlO(OH) to Al_2O_3 (Eg. 2) and simultaneous formation of protective char, compared to the $Al(OH)_3$ nanoparticles, which were transformed to Al_2O_3 with an additional phase change through the heating. In the process of films$decomposition, theATHpartic \leq s$ shell created compact char structures that acted as a heat insulator (Horrocks 2011). This reduced the thermal conductivity and the amount of released oxygen inside the material, and, due to the oxidation-reduction processes, it might absorb highly reactive radicals, which all inhibit thermal and mass flow inside the material, and, consequently, modify its course of degradation (Norouzi et al. 2015). This means that ATH nanoparticles can enhance the charring properties of the MFC matrix (He et al. 2018), and, by forming a protective layer over the MFC, protect it from further decomposition (Yuan et al. 2016).

The specific heat capacity of the prepared films was also evaluated to get information about their thermal isolation or heat transportation ability. Since heat capacity is the amount of heat required to change the temperature of one unit mass of material by one degree, and the heat capacity for any polymeric material is temperature dependent (Wen 2007), the heat capacities of the samples were measured up to 200°C before the samples underwent the accelerated phase transitions. Heat capacities for polymers are usually in the range from 0 to 3 J/gK (Wen 2007), which also corresponds to that of our samples. The lower the heat capacity, the energy in the form of heat is transferred more easily through the film, thus cooling the material passively, and acting as a thermal conductor, that is becoming an emerging demand for e.g., electronic products (Sato et al. 2020). As can be seen from the curves in Fig. 8d and specific heat capacity values collected in the inserted Table 2, the values for all samples increased with increased temperature (an exception is the sample MFC-3-ATH20p, where the values were almost constant), and decreased with the added amount of ATH nanoparticles, indicating their different insulation properties. The lowest heat capacity was observed for the highest concentration of ATH20p nanoparticles, where the value was reduced by more than ~65% compared to pure MFC film, which might be correlated to the dense and homogeneously covered cellulose fibrils with highly crystalline AlO(OH)/Al_2O_3 structured particles, which transferred the heat easily and evenly throughout the whole tested temperature region, thus acting as an efficient thermal remover by dissipating the heat. On the other hand, films prepared with more amorphous $Al(OH)_3$ based forms of ATHw nanoparticles increased the heat capacity of the films up to ~57% compared to the pure MFC at lower ATHw concentrations, and reduced it by around 22% at the highest content of larger ATH40w, which might be related to the particles` aggregation. The aggregation of particles affects the thermal conductivity, where, with increased size of agglomeration the interface between agglomerates is increased, and, consequently, leads to a reduction of thermal conductivity or decreased heat capacity (Machrafi et al. 2016). The improved heat transfer abilities of MFC-ATHp films make them a good candidate for electronic products (Sato et al. 2020). Additionally, their lower OTR values and increased hydrophobicity also makes them interesting for application in e.g., food packaged products. Packaging plays an important role in the protection of food products against a range of external influences, among which, besides oxygen and water-vapor barrier properties (Hubbe et al. 2017), temperature variations are becoming another issue that have a negative impact on keeping packaged foodstuffs fresh for longer durations (Singh et al. 2018).

4. Conclusion

Structurally and size-related different aluminum (tri/mono) hydroxide ($Al(OH)_3$ / AlO(OH)) nanoparticles were prepared and used as a thermo-stable additive to thin-layered films of microfibrillated cellulose (MFC), to create new environmentally friendly and biodegradable materials. The addition of ATH nanoparticles increased the films
$thermalstabilitysign \quad \text{if} \quad icantly, asthereseamountafterde\nabla ationgothigher, de\nabla ationtemperaturesmoved \rightarrow highervalues \text{ and } th$
optical, oxygen-barrier, mechanical, heat resistant and thermal-management properties were highly dependent on the particles` sizes and polymorphic structure, their content and distribution through the film, as well as their transformation through the heating. The smaller and meta-stable AlO(OH) particles with large surface area and gradual decomposition thus resulted to optically transparent and thermally the most stable film with higher heat transition / dissipating ability, and an increased tensile strength and Young's modulus. This showed their potential applications in flexible and transparent opto-electronics to cool the device, or in thermal sensitive packaging materials to protect the products from external heating. In addition, a hydrophobic surface with low oxygen permeability shows that such a film is also useful in eco-benign food packaging.

Declarations

Funding

This research was funded by the Slovenian Research Agency (Grant No. L2-9249 and Research Program P2-0118).

Conflicts of interest

The authors declare no conflict of interest.

References

Abdollahifar M, Hidaryan M, Jafari P (2018) The role anions on the synthesis of AlOOH nanoparticles using simple solvothermal method. Boletín de la Sociedad Española de Cerámica y Vidrio 57(2):66-72. https://doi.org/10.1016/j.bsecv.2017.06.002

Abitbol T, Rivkin A, Cao Y, Nevo Y, Abraham E, Ben-Shalom T, Lapidot S, Shoseyov O (2016) Nanocellulose, a tiny fiber with huge applications. Current Opinion in Biotechnology 3:76-88. https://doi.org/10.1016/j.copbio.2016.01.002

Acharya D, Mohanta B, Deb S, Sen A (2018) Theoretical prediction of absorbance spectra considering the particle size distribution using Mie theory and their comparison with the experimental UV–Vis spectra of synthesized nanoparticles. Spectroscopy Letters 51:1-5.

https://doi.org/10.1080/00387010.2018.1442351

Andresen M, Johansson L-S, Tanem BS, Stenius P (2006) Properties and characterization of hydrophobized microfibrillated cellulose. Cellulose 13(6):665-677. https://doi.org/10.1007/s10570-006-9072-1

Ballal D, Chapman W G (2013) Hydrophobic and hydrophilic interactions in aqueous mixtures of alcohols at a hydrophobic surface. The Journal of chemical physics 139(11):114706. https://doi.org/10.1063/1.4821604

Beeran Y P T, Bobnar V, Gorgieva S, Grohens Y, Finšgar M, Thomas S, Kokol V (2016) Mechanically strong, flexible and thermally stable graphene oxide/nanocellulosic films with enhanced dielectric properties. Rsc Advances 6(54):49138-49149. https://doi.org/10.1039/C6RA06744A

Belbekhouche S, Bras J, Siqueira G, Chappey C, Lebrun L, Khelifi B, Marais S, Dufresne A (2011) Water sorption behavior and gas barrier properties of cellulose whiskers and microfibrils films. Carbohydrate Polymers 83(4):1740-1748.

https://doi.org/10.1016/j.carbpol.2010.10.036

Beyer G (2001) Flame retardant properties of EVA-nanocomposites and improvements by combination of nanofillers with aluminium trihydrate. Fire and Materials 25(5):193-197. https://doi.org/10.1002/fam.776

Bunderšek A (2015) Influence of integration of Al(OH)3 nanoparticles on properties of cured acrylic composites. Dissertation, University of Maribor UDK: 66.095.26-97-022-17(043.3)

Bunderšek A, Japelj B, Mušič B, Rajnar N, Gyergyek S, Kostanjšek R, Krajnc P (2016) Influence of Al(OH)3 nanoparticles on the mechanical and fire resistance properties of poly(methyl methacrylate) nanocomposites. Polymer Composites 37(6):1659-1666. https://doi.org/10.1002/pc.23338

Castro D O, Karim Z, Medina L, Häggström J O, Carosio F, Svedberg A, Wågberg L, Söderberg D, Berglund L A (2018) The use of a pilot-scale continuous paper process for fire retardant cellulose-kaolinite nanocomposites. Composites Science and Technology 162:215-224. https://doi.org/10.1016/j.compscitech.2018.04.032

Chen Q, Zeng W (1996) Calorimetric determination of the standard enthalpies of formation of gibbsite, Al(OH)3(cr), and boehmite, AlOOH(cr). Geochimica et Cosmochimica Acta 60(1):1-5. https://doi.org/10.1016/0016-7037(95)00378-9

Cox J D, Wagman D D, Medvedev V A (1990) CODATA - Key Values for Thermodynamics. CODATA, Series on Thermodynamic Properties. Hemisphere Publishing Corporation, New York

Da Silva M A, Calabrese V, Schmitt J, Celebi D, Scott J L, Edler K J (2018) Alcohol induced gelation of TEMPO-oxidized cellulose nanofibril dispersions. Soft Matter 14(45):9243-9249. https://doi.org/10.1039/C8SM01815D

De Salvi D T B, Barud H S, Caiut J M A, Messaddeq Y, Ribeiro S J L (2012) Self-supported bacterial cellulose/boehmite organic–inorganic hybrid films. Journal of Sol-Gel Science and Technology 63:211-218. https://doi.org/10.1007/s10971-012-2678-x

Du X, Zhang Z, Liu W, Deng Y (2017) Nanocellulose-based conductive materials and their emerging applications in energy devices-A review. Nano Energy 35:299-320. https://doi.org/10.1016/j.nanoen.2017.04.001

Dufresne A (2013) Nanocellulose: a new ageless bionanomaterial. Materials Today 16(6):220-227. https://doi.org/10.1016/j.mattod.2013.06.004

Farooq M, Sipponen M H, Seppälä A, Österberg M (2018) Eco-friendly flame-retardant cellulose nanofibril aerogels by incorporating sodium bicarbonate. ACS Applied Materials & Interfaces 10(32):27407-27415. https://doi.org/10.1021/acsami.8b04376

Favaro L, Boumaza A, Roy P, Lédion J, Sattonnay G, Brubach J B, Huntz A, TÉTot R (2010) Experimental and ab initio infrared study of χ-, κ- and α-aluminas formed from gibbsite. Journal of Solid State Chemistry 183:901-908. 10.1016/j.jssc.2010.02.010

Ghanadpour M, Wicklein B, Carosio F, Wågberg L (2018) All-natural and highly flame-resistant freeze-cast foams based on phosphorylated cellulose nanofibrils. *Nanoscale* 10(8):4085-4095. https://doi.org/10.1039/C7NR09243A

Gopakumar D A, Pai A R, Pottathara Y B, Pasquini D, de Morais L C, Luke M, Kalarikkal N, Grohens Y, Thomas S (2018) Cellulose nanofiber-based polyaniline flexible papers as sustainable microwave absorbers in the X-Band. ACS Applied Materials & Interfaces 10(23):20032-20043. https://doi.org/10.1021/acsami.8b04549

Gorgieva S, Jančič U, Hribernik S, Fakin D, Stana Kleinschek K, Medved S, Fakin T, Božič M (2020) Processing and functional assessment of anisotropic cellulose nanofibril/Alolt/sodium silicate: based aerogels as flame retardant thermal insulators. Cellulose 27(3):1661-1683. https://doi.org/10.1007/s10570-019-02901-3

Goudarzi M, Ghanbari D, Salavati-Niasari M, Ahmadi A (2016) Synthesis and Characterization of Al(OH)3, Al2O3 Nanoparticles and Polymeric Nanocomposites. Journal of Cluster Science 27(1):25-38. https://doi.org/10.1007/s10876-015-0895-5

Guo W, Wang X, Zhang P, Liu J, Song L, Hu Y (2018) Nano-fibrillated cellulose-hydroxyapatite based composite foams with excellent fire resistance. Carbohydrate Polymers 195:71-78. https://doi.org/10.1016/j.carbpol.2018.04.063

He C, Huang J, Li S, Meng K, Zhang L, Chen Z, Lai Y (2018) Mechanically resistant and sustainable cellulose-based composite aerogels with excellent flame retardant, sound-absorption, and superantiwetting ability for advanced engineering materials. ACS Sustainable Chemistry & Engineering 6(1):927-936. https://doi.org/10.1021/acssuschemeng.7b03281

Horrocks A R (2011) Flame retardant challenges for textiles and fibres: New chemistry versus innovatory solutions. Polymer Degradation and Stability 96(3):377-392. https://doi.org/10.1016/j.polymdegradstab.2010.03.036

Hubbe M A, Ferrer A, Tyagi P, Yin Y, Salas C, Pal L, Rojas O (2017) Nanocellulose in thin films, coatings, and plies for packaging applications: A review. BioResources 12(1):2143-2233. http://urn.fi/URN:NBN:fi:aalto-201710157155

Hull T R, Witkowski A, Hollingbery L (2011) Fire retardant action of mineral fillers. Polymer Degradation and Stability 96(8):1462-1469. https://doi.org/10.1016/j.polymdegradstab.2011.05.006

Jiang L, Li K, Yang H, Liu X, Xu W, Deng B (2019) Significantly improved flame-retardancy of cellulose acetate nanofiber by Mg-based nano flaky petal. Cellulose 26:5211-5226. https://doi.org/10.1007/s10570-019-02451-8

Jin S, Li K, Li J (2018) Nature-inspired green procedure for improving performance of protein-based nanocomposites via introduction of nanofibrillated cellulose-stablized graphene/carbon nanotubes hybrid. Polymers 10(3):270. https://doi.org/10.3390/polym10030270

Karger-Kocsis J, Lendvai L (2018) Polymer/boehmite nanocomposites: A review. Journal of Applied Polymer Science 135(24):45573. https://doi.org/10.1002/app.45573

Kaushik M, Moores A (2016) Review: nanocelluloses as versatile supports for metal nanoparticles and their applications in catalysis. Green Chemistry 18(3):622-637. https://doi.org/10.1039/C5GC02500A

Kim, J-H, Lee D, Lee Y-H, Chen W, Lee S-Y (2019) Nanocellulose for energy storage systems: beyond the limits of synthetic materials. Advanced Materials 31(20):1804826. https://doi.org/10.1002/adma.201804826

Köklükaya O, Carosio F, Wågberg L (2017) Superior flame-resistant cellulose nanofibril aerogels modified with hybrid layer-by-layer coatings. ACS Applied Materials & Interfaces 9(34):29082-29092. https://doi.org/10.1021/acsami.7b08018

Lamouri S, Hamidouche M, Bouaouadja N, Belhouchet H, Garnier V, Fantozzi G, Trelkat J F (2017) Control of the γ-alumina to α-alumina phase transformation for an optimized alumina densification. Boletín de la Sociedad Española de Cerámica y Vidrio 56(2):47-54. https://doi.org/10.1016/j.bsecv.2016.10.001

Laoutid F, Bonnaud L, Alexandre M, Lopez-Cuesta J M, Dubois P (2009) New prospects in flame retardant polymer materials: From fundamentals to nanocomposites. Materials Science and Engineering: R: Reports 63(3):100-125. https://doi.org/10.1016/j.mser.2008.09.002

Li Y, Wang B, Sui X, Xu H, Zhang L, Zhong Y, Mao Z (2017) Facile synthesis of microfibrillated cellulose/organosilicon/polydopamine composite sponges with flame retardant properties. Cellulose 24(9):3815-3823. https://doi.org/10.1007/s10570-017-1373-z

Lichtenstein K, Lavoine N (2017) Toward a deeper understanding of the thermal degradation mechanism of nanocellulose. Polymer Degradation and Stability 146:53-60. https://doi.org/10.1016/j.polymdegradstab.2017.09.018

Lin W, Hu X, You X, Sun Y, Wen Y, Yang W, Zhang X, Li Y, Chen H (2018) Hydrophobic modification of nanocellulose via a two-step silanation method. Polymers 10(9):1035. https://doi.org/10.3390/polym10091035

Lu J, Askeland P, Drzal L T (2008) Surface modification of microfibrillated cellulose for epoxy composite applications. Polymer 49(5):1285-1296. https://doi.org/10.1016/j.polymer.2008.01.028

Machrafi H, Lebon G, Iorio C S (2016) Effect of volume-fraction dependent agglomeration of nanoparticles on the thermal conductivity of nanocomposites: Applications to epoxy resins, filled by SiO2, AlN and MgO nanoparticles. Composites Science and Technology 130:78-87. https://doi.org/10.1016/j.compscitech.2016.05.003

Mastalska-Popławska J, Pernechele M, Troczynski T, Izak P (2017) Thermal properties of silica-coated cellulose fibers for increased fire-resistance. Journal of Sol-Gel Science Technology 83(3):683-691. https://doi.org/10.1007/s10971-017-4445-5

Miyashiro D, Hamano R, Umemura U (2020) A review of applications using mixed materials of cellulose, nanocellulose and carbon nanotubes. Nanomaterials 10(2):186. https://doi.org/10.3390/nano10020186

Norouzi M, Zare Y, Kiany P (2015) Nanoparticles as effective flame retardants for natural and synthetic textile polymers: application, mechanism, and optimization. Polymer Reviews 55(3):531-560. https://doi.org/10.1080/15583724.2014.980427

Oun A A, Shankar S, Rhim J-W (2020) Multifunctional nanocellulose/metal and metal oxide nanoparticle hybrid nanomaterials. Critical Reviews in Food Science and Nutrition 60(3):435-460. https://doi.org/10.1080/10408398.2018.1536966

Rahmanpour O, Shariati A, Khosravi-Nikou M R (2012) New Method for Synthesis Nano Size γ-Al2O3 Catalyst for Dehydration of Methanol to Dimethyl Ether. International Journal of Chemical Engineering and Applications 3(2):125-128. 10.7763/IJCEA.2012.V3.172

Reddy T, Thyagarajan K, Almanza O, Sanapa-Reddy L, Endo T (2014) X-Ray Diffraction, Electron Paramagnetic Resonance and Optical Absorption Study of Bauxite. Journal of Minerals and Materials Characterization and Engineering 2:114-120. http://dx.doi.org/10.4236/jmmce.2014.22015

Sato K, Tominaga Y, Imai Y (2020) Nanocellulose and related materials applicable in thermal management of eletronic devices: A review. Nanomaterials 10(3):448-459.

https://doi.org/10.3390/nano10030448

Sathish S, Chandar Shrekar B, Chandru Kannan S, Sengodan R, Dinesh K, Ranjithkumar R (2015) Wide band gap transparent polymer-inorganic composite thin films by dip-coating method: Preparation and Characterizations. International Journal of Polymer Analysis and Characterization 20(1):29-41. https://doi.org/10.1080/1023666X.2015.975414

Schawe J E K, Hütter T, Heitz C, Alig I, Lellinger D (2006) Stochastic temperature modulation: A new technique in temperature-modulated DSC. Thermochimica Acta 446(1-2):147-155. https://doi.org/10.1016/j.tca.2006.01.031

Sifontes A, Gutiérrez B, Mónaco A, Yanez A, Diaz Y, Mendez F, Llovera L, Cañizales E, Brito J (2014) Preparation of funcionalized porous nano-γ-Al2O3 powders employing colophony extract. Biotechnology Reports 4:21-29. http://dx.doi.org/10.1016/j.btre.2014.07.001

Sing KS (1985) Reporting physisorption data for gas/solid systems with special reference to the determination of surface area and porosity (Recommendations 1984). Pure and applied chemistry 57(4):603-619. https://doi.org/10.1351/pac198557040603

Singh S, Gaikwad K K, Lee M, Lee Z S (2018) Temperature-regulating materials for advanced food packaging applications: a review. Journal of Food Measurement and Characterization 12:588-601. https://doi.org/10.1007/s11694-017-9672-5

Wang L, Cui L, Sánchez-Soto M, Shou W, Xia Z, Liu Y (2018) Highly flame retardant melamine-formaldehyde cross-linked cellulose nanofibrils/sodium montmorillonite aerogels with improved mechanical properties. Macromolecular Materials and Engineering 303(10):1800379. https://doi.org/10.1002/mame.201800379

Wen J (2007) Heat Capacities of Polymers. In: Mark JE (ed) Physical properties of polymers Handbook. SpringerMaterials, New York, pp 145-154. https://materials.springer.com/lb/docs/sm_nlb_978-0-387-69002-5_9

Wicklein B, Kocjan A, Salazar-Alvarez G, Carosio F, Camino G, Antonietti M, Bergström L (2014) Thermally insulating and fire-retardant lightweight anisotropic foams based on nanocellulose and graphene oxide. Nature Nanotechnology 10:277-283. https://doi.org/10.1038/nnano.2014.248

Wu C-N, Saito T, Yang Q, Fukuzumi H, Isogai A (2014) Increase in the water contact angle of composite film surfaces caused by the assembly of hydrophilic nanocellulose fibrils and nanoclay platelets. ACS Applied Materials & Interfaces 6(15):12707-12712. https://doi.org/10.1021/am502701e

Yang F, Zhang Y, Feng Y (2017) Adding aluminum hydroxide to plant fibers using in situ precipitation to improve heat resistance. BioResources 12(1):1826-1834. doi:10.15376/biores.12.1.1826-1834

Yang S, Xie Q, Liu X, Wu M, Wang S, Song X (2018) Acetylation improves thermal stability and transmittance in FOLED substrates based on nanocellulose films. RSC Advances 8(7):3619-3625. https://doi.org/10.1039/C7RA11134G

Yuan B, Zhang J, Yu J, Song R, Mi Q, He J, Zhang J (2016) Transparent and flame retardant cellulose/aluminum hydroxide nanocomposite aerogels. Science China Chemistry 59(10):1335-1341. https://doi.org/10.1007/s11426-016-0188-0

Zeng Z, Wu T, Han D, Ren Q, Siqueira G, Nyström G (2020) Ultralight, flexible, and biomimetic nanocellulose/silver nanowire aerogels for electromagnetic interference shielding. ACS Nano 14(3):2927-2938. https://doi.org/10.1021/acsnano.9b07452

Zhang T, Zhao X, Poon R, Clifford A, Mathews R, Zhitomirsky I (2017) Synthesis and liquid-liquid extraction of non-agglomerated Al(OH)3 particles for deposition of cellulose matrix composite films. Journal of colloid and interface science 508:49-55. https://doi.org/10.1016/j.jcis.2017.08.026

Figures

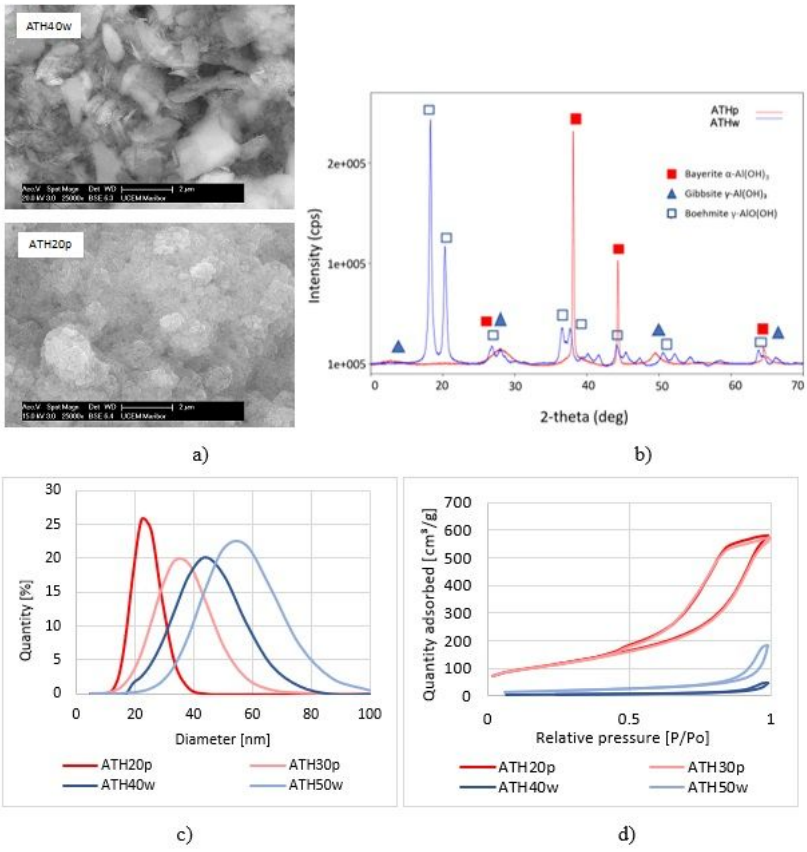

Figure 1

a) SEM imaging, b) XRD patterns, c) Size distribution curves measured by DLS, and d) BETN adsorption-desorption isotherms of differently prepared ATH nanoparticles.

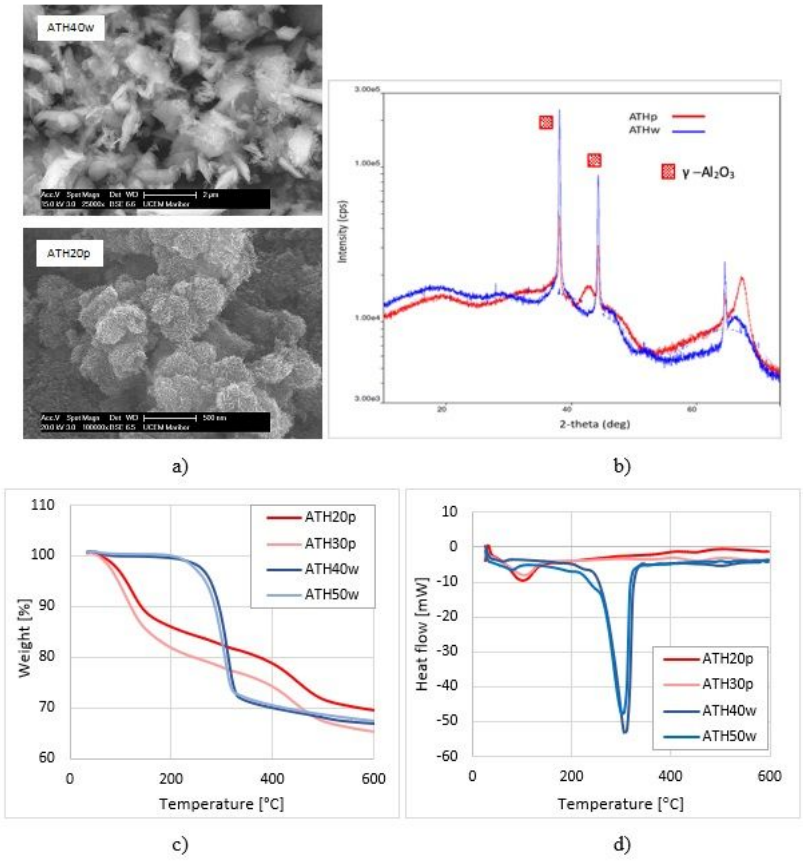

Figure 2

a) SEM images and b) XRD analysis after thermal degradation of ATH NPs, c) TGA and d) DSC analysis of differently prepared ATH nanoparticles,

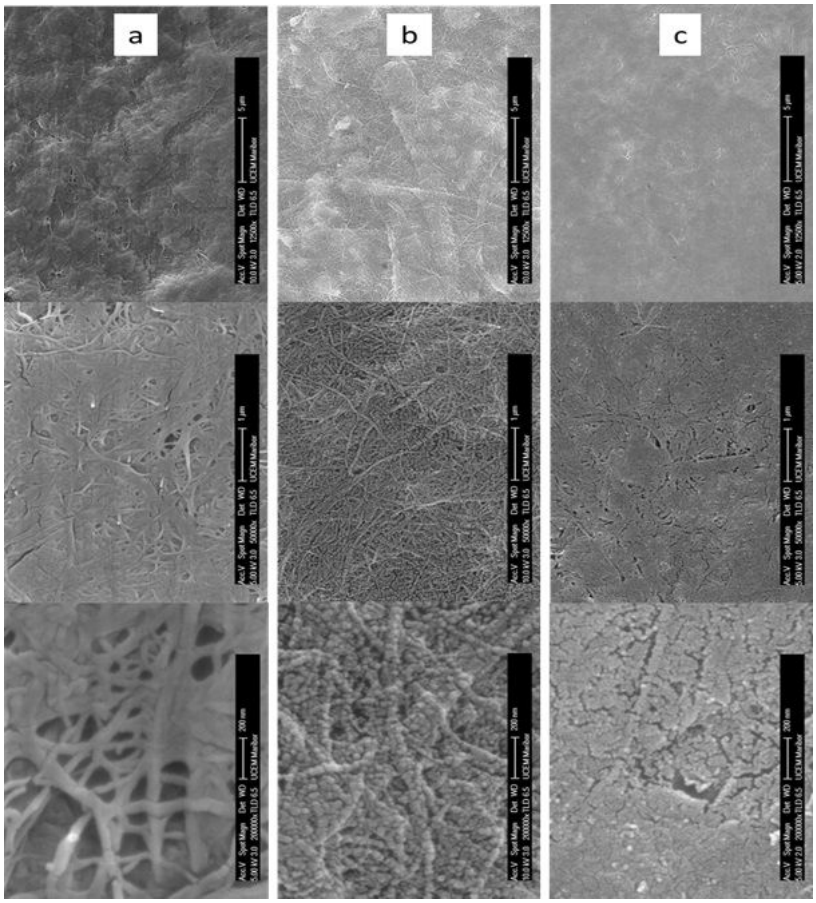

Figure 3

SEM images of film surfaces prepared from a) MFC, and MFC with the addition of 50 w/w% of differently prepared ATH nanoparticles: b) ATH40w and c) ATH20p.

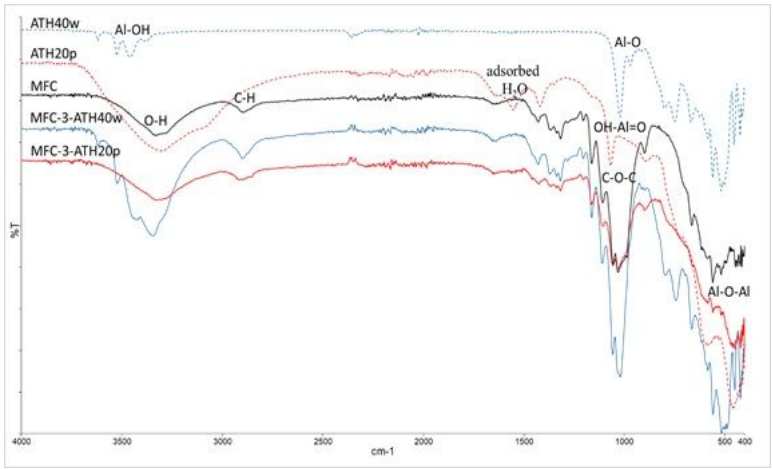

Figure 4

FTIR spectrum of ATH40w and ATH20p nanoparticles and MFC films with and without the addition of 50 w/w% of nanoparticles.

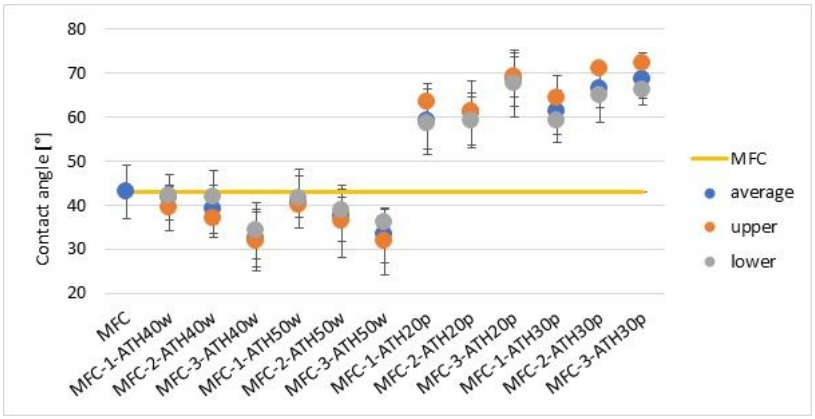

Figure 5

Contact Angle values of different MFC-based films, measured on the upper / air-turned and lower / Petri-turned sides.

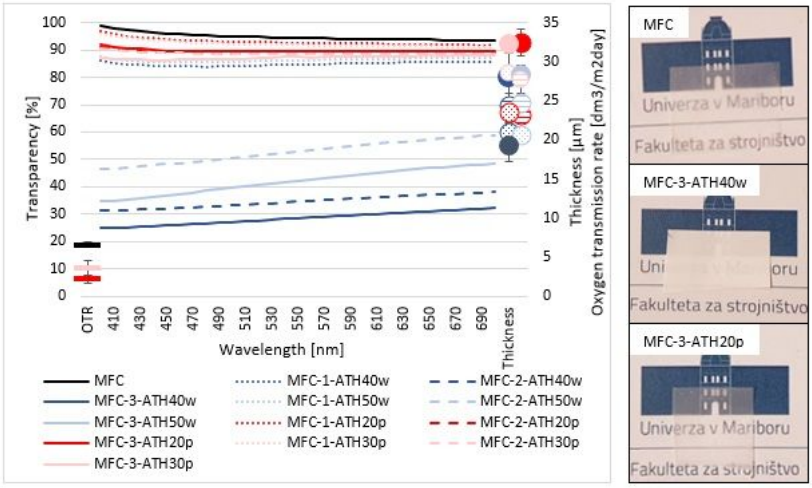

Figure 6

Thickness, Transmittance and OTR values of different MFC-based films (left); photographic images of films showing their transparency (right).

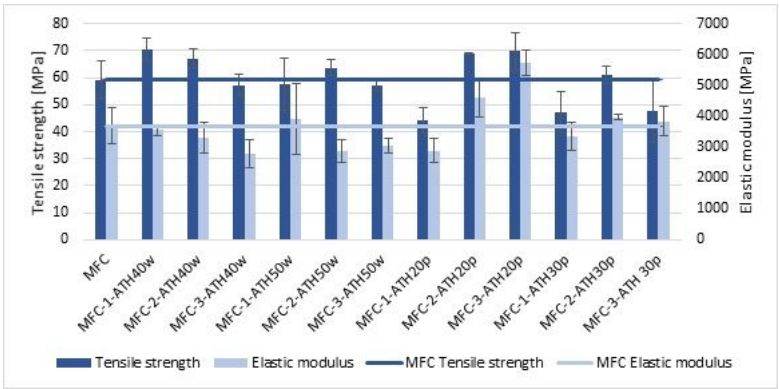

Figure 7

Tensile strength and elastic modulus of different MFC-based films.

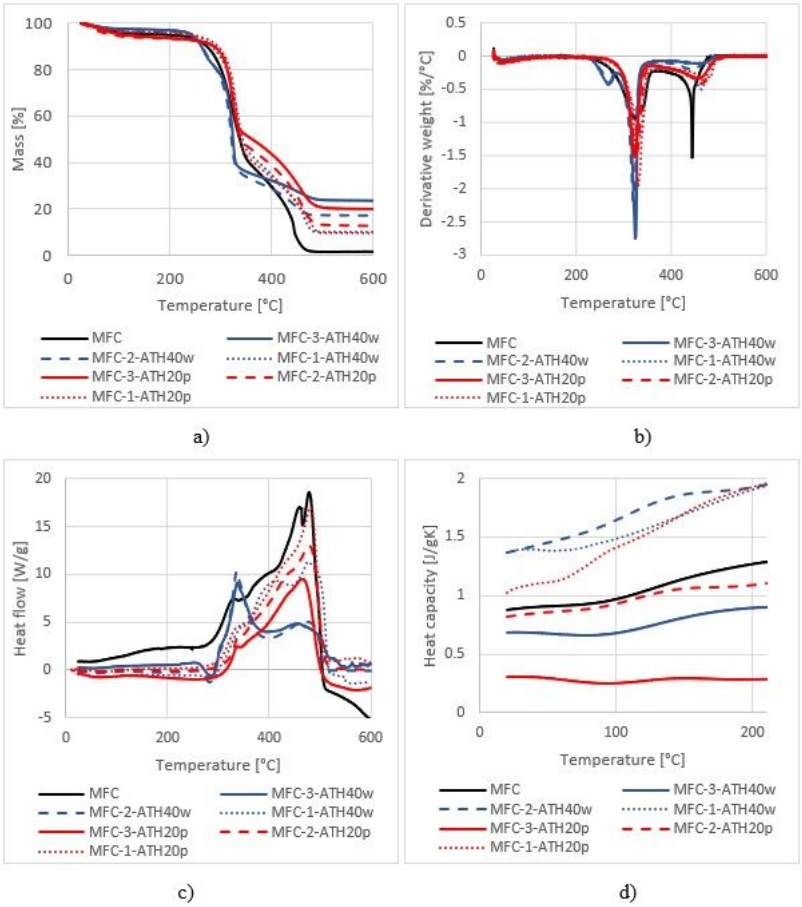

Figure 8

a) Thermo-gravimetric (TG), b) Derivative weight (DTG) c) Heat-flow (DSC) analysis and d) Heat-capacity curves of different MFC-based films.